



ARL-CR-0792 • JAN 2016



Quantifying Discretization Effects on Brain Trauma Simulations

prepared by Sophia M Haire
American Society for Engineering Education
1818 N St NW, #600
Washington, DC 20036

under contract W911NF-10-2-0076

Approved for public release; distribution is unlimited.

NOTICES

Disclaimers

The findings in this report are not to be construed as an official Department of the Army position unless so designated by other authorized documents.

Citation of manufacturer's or trade names does not constitute an official endorsement or approval of the use thereof.

Destroy this report when it is no longer needed. Do not return it to the originator.



Quantifying Discretization Effects on Brain Trauma Simulations

prepared by Sophia M Haire

American Society for Engineering Education

1818 N St NW, #600

Washington, DC 20036

under contract W911NF-10-2-0076

REPORT DOCUMENTATION PAGE				Form Approved OMB No. 0704-0188	
<p>Public reporting burden for this collection of information is estimated to average 1 hour per response, including the time for reviewing instructions, searching existing data sources, gathering and maintaining the data needed, and completing and reviewing the collection information. Send comments regarding this burden estimate or any other aspect of this collection of information, including suggestions for reducing the burden, to Department of Defense, Washington Headquarters Services, Directorate for Information Operations and Reports (0704-0188), 1215 Jefferson Davis Highway, Suite 1204, Arlington, VA 22202-4302. Respondents should be aware that notwithstanding any other provision of law, no person shall be subject to any penalty for failing to comply with a collection of information if it does not display a currently valid OMB control number.</p> <p>PLEASE DO NOT RETURN YOUR FORM TO THE ABOVE ADDRESS.</p>					
1. REPORT DATE (DD-MM-YYYY)		2. REPORT TYPE		3. DATES COVERED (From - To)	
January 2016		Final		June 2015–August 2015	
4. TITLE AND SUBTITLE Quantifying Discretization Effects on Brain Trauma Simulations				5a. CONTRACT NUMBER	
				W911NF-10-2-0076	
				5b. GRANT NUMBER	
6. AUTHOR(S) Sophia M Haire				5c. PROGRAM ELEMENT NUMBER	
				5d. PROJECT NUMBER	
7. PERFORMING ORGANIZATION NAME(S) AND ADDRESS(ES) American Society for Engineering Education 1818 N St NW, #600 Washington, DC 20036				622618H80	
				5e. TASK NUMBER	
				5f. WORK UNIT NUMBER	
8. PERFORMING ORGANIZATION REPORT NUMBER					
9. SPONSORING/MONITORING AGENCY NAME(S) AND ADDRESS(ES) US Army Research Laboratory ATTN: RDRL-WMP-C Aberdeen Proving Ground, MD 21005-5069				10. SPONSOR/MONITOR'S ACRONYM(S)	
				11. SPONSOR/MONITOR'S REPORT NUMBER(S)	
				ARL-CR-0792	
12. DISTRIBUTION/AVAILABILITY STATEMENT Approved for public release; distribution is unlimited.					
13. SUPPLEMENTARY NOTES					
14. ABSTRACT Numerical models of the brain are becoming an important tool for developing protective headgear for the Soldier. One nonphysical parameter that is often taken for granted in these models is the material representation by the mesh; arbitrarily formed meshes can propagate error when resolving interactions among the skull, cerebrospinal fluid, and brain. We compared Lagrangian, pure Eulerian, and embedded Lagrangian/Eulerian schemes under both 2-dimensional cyclic rotation and planar blast scenarios. The 3 discretization techniques used differ not only in their finite element implementations but also necessarily in their representations of cerebrospinal fluid. The quantities analyzed in each case were the variations in stress magnitude, spatial distribution, and wave patterns that arise inside the brain. The effects of various time scales, degrees of rotation, and mesh resolutions were compared across methodologies to quantify the solutions and efficiencies of each technique and to understand how their formulations contribute to results. Preliminary results show that the wave patterns and spatial distributions for the rotational simulations are significantly different among the methodologies and that there is much more agreement among the blast loading simulations. Further investigation into specific aspects of several of the models is recommended.					
15. SUBJECT TERMS mesh effect, finite element, brain, interface, sliding					
16. SECURITY CLASSIFICATION OF:			17. LIMITATION OF ABSTRACT UU	18. NUMBER OF PAGES 48	19a. NAME OF RESPONSIBLE PERSON
a. REPORT Unclassified	b. ABSTRACT Unclassified	c. THIS PAGE Unclassified			Richard C Becker
					19b. TELEPHONE NUMBER (Include area code) 410-278-7980

Contents

List of Figures	iv
List of Tables	v
Acknowledgments	vi
Student Bio	vii
1. Introduction and Background	1
2. Methods	1
3. Rotational Model Analysis	9
3.1 Results across Discretization Methods	9
3.2 Effects of Mesh Resolution on Results	14
3.3 Efficiency Analysis	20
4. Blast Loading Model Analysis	21
4.1 Results across Discretization Methods	21
4.2 Effects of Mesh Resolution on Results	25
4.3 Efficiency Analysis	31
5. Conclusions and Recommendations	31
6. References	33
Appendix. Material Parameters	35
Distribution List	38

List of Figures

Fig. 1	Example meshes for each discretization case. The meshes shown use Lagrangian, Eulerian, and embedded methods from top to bottom.....	3
Fig. 2	Loading node-set for Eulerian rotational problem. The dark shaded area around the skull is the area to which the angular velocity loading was applied.....	4
Fig. 3	Load curve for rotational models	5
Fig. 4	Velocity, energy, and density inflow conditions for planar blast loading problem	6
Fig. 5	Example of planar blast loading problem. The dimensions of the air in the simulation are 900 mm in the x-direction by 450 mm in the y-direction. The example shown is pure Eulerian.....	7
Fig. 6	Locations of tracer particles. The particles are located 5, 20, and 50 mm in from the right and top inner edges of the skull. The example shown is a Lagrangian rotational model. The red and green materials represent the brain and skull, respectively.	8
Fig. 7	Effect of discretization method on pressure distribution. The rotation angles shown are 10.1° from equilibrium, 0.9° back toward equilibrium from the inflection point (displaced 59.1° from equilibrium), and 44.3° back toward equilibrium from the inflection point (displaced 15.7° from equilibrium).	10
Fig. 8	Effect of discretization method on von Mises equivalent stress distribution. Like in Fig. 7, the rotation angles shown are 10.1° from equilibrium, 0.9° back toward equilibrium from the inflection point (displaced 59.1° from equilibrium), and 44.3° back toward equilibrium from the inflection point (displaced 15.7° from equilibrium).....	11
Fig. 9	Effect of discretization method on effective strain distribution. Like in Figs. 7 and 8, the rotation angles shown are 10.1° from equilibrium, 0.9° back toward equilibrium from the inflection point (displaced 59.1° from equilibrium), and 44.3° back toward equilibrium from the inflection point (displaced 15.7° from equilibrium).	12
Fig. 10	Distance between master and slave nodes over time	13
Fig. 11	Pressure over time by mesh resolution at 3 tracer locations, Lagrangian model. The graph legends indicate the number of elements used in each simulation. The red dashed lines display the inflection points in the simulation—that is, the approximate points at which the velocity changed directions. Data points were collected every 1.0 ms.	15

Fig. 12	Pressure over time by mesh resolution at 3 tracer locations, Eulerian model. As in Fig. 11, the graph legends indicate the number of elements used in each simulation, and the red dashed lines display the inflection points in the simulation—that is, the approximate points at which the velocity changed directions. Data points were collected every 1.0 ms.	17
Fig. 13	Pressure over time by mesh resolution at 3 tracer locations, embedded model. As in Figs. 11 and 12, the graph legends indicate the number of elements used in each simulation. Data points were collected every 1.0 ms.	19
Fig. 14	Wall time by mesh resolution of Lagrangian and Eulerian methods, rotational models.....	20
Fig. 15	Pressure over time by discretization method at 6 tracer locations, highest resolution. The number of elements in the Eulerian, embedded, and Lagrangian simulations are 2,531,250; 2,532,018; and 311,994; respectively. Data points were collected every 1.0 ms.	22
Fig. 16	Pressure over time by mesh resolution at 3 tracer locations, Eulerian blast model. The graph legends indicate the number of elements used in each simulation. Data points were collected every 1.0 ms.	26
Fig. 17	Pressure over time by mesh resolution at 3 tracer locations, embedded blast model. The graph legends indicate the number of elements used in each simulation. Data points were collected every 1.0 ms.	28
Fig. 18	Pressure over time by mesh resolution at 3 tracer locations, Lagrangian blast model. The graph legends indicate the number of elements used in each simulation. Data points were collected every 1.0 ms.	30
Fig. 19	Wall time by mesh resolution of each discretization method, blast models. For clarity, a projected linear trend curve is included for the Lagrangian model.	31

List of Tables

Table.	Average element sizes within the head by simulation	9
--------	---	---

Acknowledgments

The author wishes to acknowledge the mentorship, support, and patience of Dr Richard Becker. Funding for this project was provided by the Blast Protection for Platforms and Personnel Institute.

Student Bio

Sophia M Haire is a junior studying computer science and mathematics at the University of Maryland, Baltimore County. The summer of 2015 marked her second internship with the US Army Research Laboratory (ARL); her previous work consisted of software development and production for ARL shadowgraph range data collection. Her primary career and research goals lie in the fields of human-centered computing with a focus on assisting patients with brain disorders or injuries, including the elderly.

INTENTIONALLY LEFT BLANK.

1. Introduction and Background

The Soldier Protection Sciences Branch of the US Army Research Laboratory (ARL) relies heavily on numerical models of the brain and surrounding tissues to understand load distributions, which will allow the design of efficient and effective protective equipment for the Army. A recent study of interest to the ARL community used both 2- and 3-dimensional (2-D) and (3-D) models to simulate the pressures and velocities within the brain when it was cyclically rotated about the axis of the neck at a targeted rate.¹ The models, meshed using Eulerian (fixed-grid) particle-based methods in the code Uintah, were validated via an experiment in which human subjects laid down, placed their heads in a device, and rotated their heads back and forth; tagged MRI was used to collect relevant data. Although the magnitudes and propagation of velocities between the empirical data and simulated results in the study were similar, the predicted pressure distribution in the brain was shifted in the results of the human experiments. Noticing that the complicated interface between the brain, cerebrospinal fluid (CSF), and skull was not well resolved in the study (properties were averaged among the 3 materials along the boundary), we hypothesized that the discretization scheme may skew such results. Our objective in this study is to quantify the effects that discretization methodology has on such model results by creating and analyzing a 2-D brain model with simplified geometry under 3 different discretization schemes and thus under 3 different methods of resolving the brain/CSF/skull interface. We conducted our study using both rotational boundary conditions and a planar blast-loading boundary condition for each discretization case.

2. Methods

To create models of the skull, cerebrospinal fluid, and brain, we relied on the software ALE3D from Lawrence Livermore National Laboratories.² ALE3D possesses an internal mesh generator that allows finite element meshes to be created and simulations run in Lagrangian, Eulerian, Arbitrary Lagrangian/Eulerian (ALE), and embedded Lagrangian/Eulerian schemes. In a Lagrangian simulation, the mesh is tied to the material as it moves or deforms; Eulerian simulations keep the mesh fixed while allowing material to advect through it; ALE methods move the mesh independently from the material motion, often depending on how distorted the mesh becomes over time; and the newly developed embedded method (implemented via the ALE3D FEusion package) allows coupling of fully Lagrangian and fully Eulerian objects within the same simulation.

We simplified the geometry of our brain model by reducing its shape to a 2-D ellipse with a semi-major axis of approximately 103 mm and a semi-minor axis of 83 mm, surrounded by a 7-mm-thick skull. For the Lagrangian model, the CSF was accounted for using a frictionless laminar slide surface between the brain and skull. The Eulerian model contained a 1-mm-thick CSF layer that was incorporated via mixed material zones in the mesh; in mixed material zones, material properties are averaged by volume in each element that contains multiple materials, and the boundaries between materials are reconstructed after each time step based on volume fractions. The embedded model comprises a Lagrangian skull and a Eulerian brain, and the CSF was represented via a frictionless slide surface between the two. In the pure Lagrangian and pure Eulerian rotational models, a void background was used due to the added simplicity it gave to the problem; in all other cases, a Eulerian mesh of air was used as the background. The Lagrangian blast loading problem required that embedded methodology be used to resolve the boundary between the air and the head. Figure 1 gives examples of each discretization type.

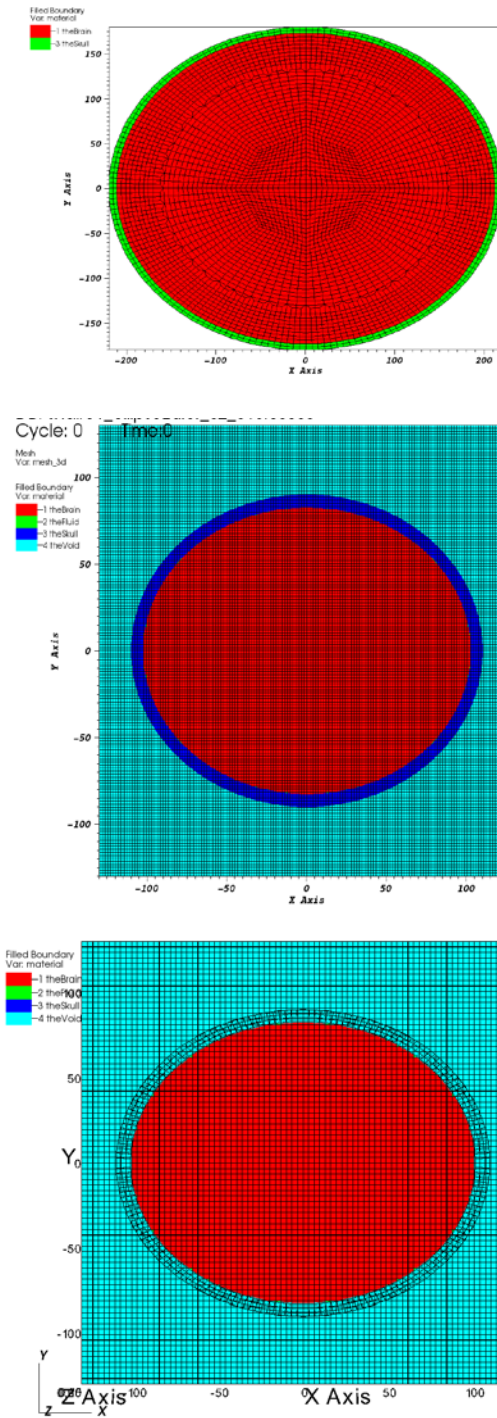


Fig. 1 Example meshes for each discretization case. The meshes shown use Lagrangian, Eulerian, and embedded methods from top to bottom.

The material properties for the air, CSF, brain, and skull were obtained from Dr Yolin Huang.³ The air was modeled as a gamma law gas with coefficient $(\gamma - 1) = 0.4$. The brain was modeled as an incompressible Mooney-Rivlin material with the follow equation of state for Cauchy stress:

$$\sigma' = \frac{\mu_0}{J} \left[\omega \tilde{B}' - (1 - \omega) (\tilde{B}^{-1})' \right] = \frac{\mu_0}{J} \left[\omega \tilde{B}' - (1 - \omega) ((\tilde{B}^2)' - \text{tr}(\tilde{B}) \tilde{B}') \right]. \quad (1)$$

The skull model used was a linear elastic model with a shear modulus of 2,660 MPa and a bulk modulus of 3,891 MPa. The units used throughout our simulations for material properties, coordinates, and results were based on grams (g), millimeters (mm), milliseconds (ms), and megapascals (MPa). These are different than the units traditionally used with ALE3D for blast simulations.

The head meshes in the rotational models were rotated using an angular velocity load curve applied to a node-set on the skull. In the Lagrangian model, the node-set chosen was the very outside surface of the skull. In the embedded simulation, all sets of nodes inside the skull except for the inner and outer surfaces of the skull were used. The Eulerian model used a filled circular mesh object that surrounded the skull and was made of the same material as the skull to rotate the head by applying the angular velocity load curve to the set of all nodes within a circular radius outside of the skull but within the circular object (Fig. 2). This method of rotation was used because the Eulerian method prevented rotation of a noncircular node-set.

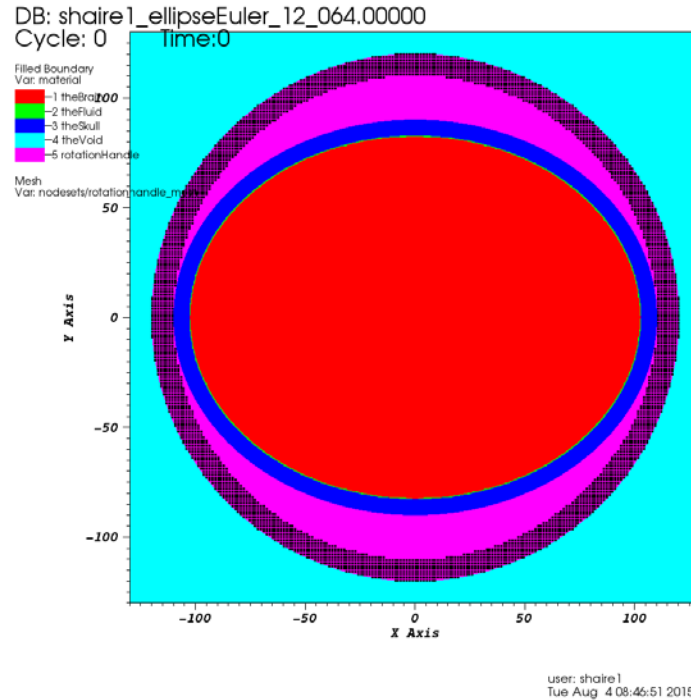


Fig. 2 Loading node-set for Eulerian rotational problem. The dark shaded area around the skull is the area to which the angular velocity loading was applied.

To evaluate our rotational models, we ran each simulation for 520.0 ms with a loading curve represented by Fig. 3. In this time, the head rotates 60° to the left, 120° to the right, and 60° left back to the center position. The rate was selected based upon android research performed by Robert Fitzpatrick,⁴ which suggested that the maximum rate of safe rotation of a human head is 467°/s. For the embedded grid simulations, we were only able to run the model for 40.0 ms as opposed to 520.0 ms because of the long run time of the simulations; so the loading curve, although the same shape as the one for the other 2 models, produced much higher velocities. Because of the time constraints of the project, no attempt was made to optimize the run time of the simulations. The 3-dimensionality of the embedded simulations and the Lagrangian blast simulation did not appear to significantly affect run time.

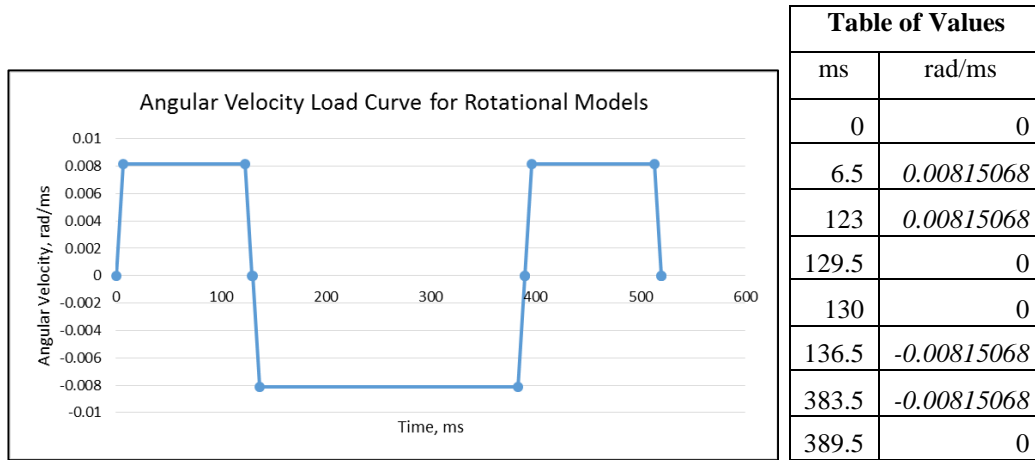


Fig. 3 Load curve for rotational models

The force applied in the blast loading models was simulated by applying velocity, density, and energy inflow conditions to the air node-set on the extreme left edge of the model, 340 mm to the left of the outer left-most edge of the skull. The inflow conditions were obtained by collecting time history values from a modified version of Dr Joel Stewart's ShockTube model, which simulated a TNT explosion initiated at the apex of a rigid right-circular cone that was 14 m long.⁵ The time histories were collected 2 m radially inward from the widest part of the cone and approximately halfway between the top edge of the cone and the midpoint axis of the cone in the vertical direction. The ShockTube simulation ran for 5.0 ms, and time histories were collected throughout the simulation. The time history data used were then restricted to the time in which a blast was actively moving past our selected tracer particle location.

Our blast loading simulations were thus run for 2.5 ms. Figure 4 depicts the inflow conditions used.

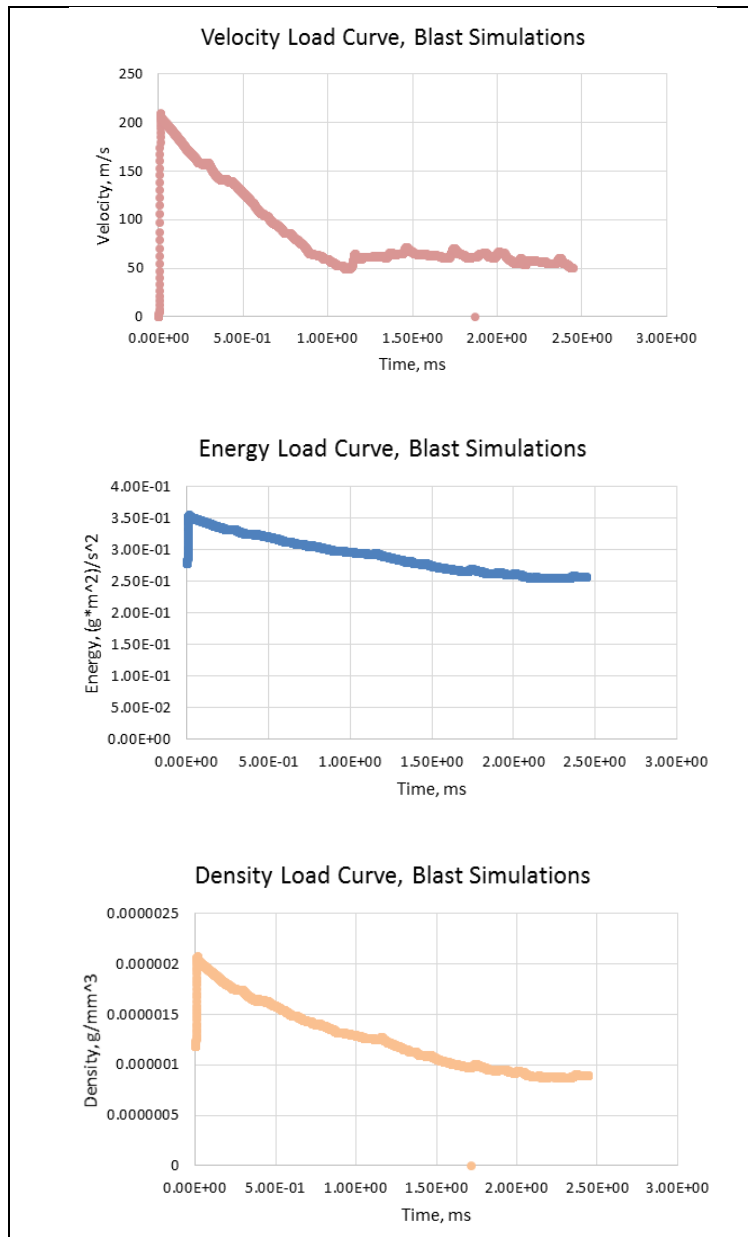


Fig. 4 Velocity, energy, and density inflow conditions for planar blast loading problem

Because of the planar symmetry of the blast loading problems, the problem was cut in half along the head's major axis, and only the upper half of the problem was run (Fig. 5).

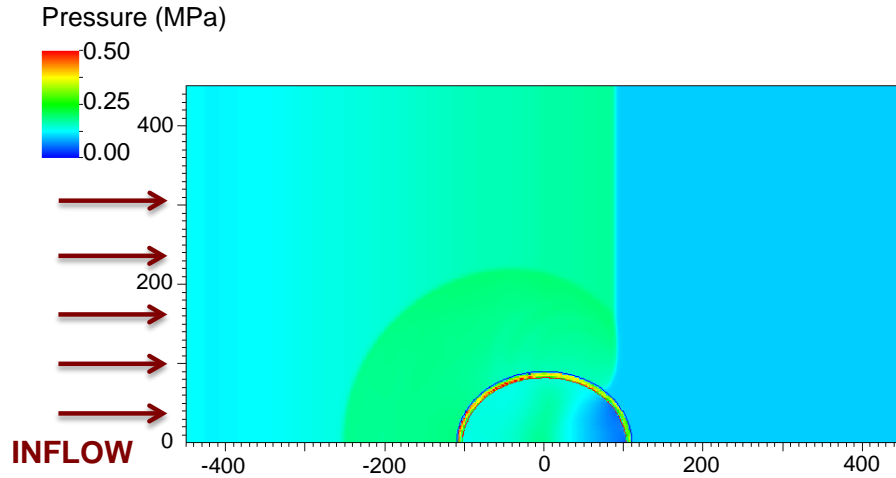


Fig. 5 Example of planar blast loading problem. The dimensions of the air in the simulation are 900 mm in the x-direction by 450 mm in the y-direction. The example shown is pure Eulerian.

Data collection was performed using 6 tracer particles located at different locations inside the brain in each mesh; the locations of the tracer particles are shown in Fig. 6. For the purposes of our simulations, the right side of the brain is the side of the brain closest to the right side of the screen when viewed in a postprocessor during the first time cycle. The top side of the brain is the side closest to the top of the screen when viewed in a postprocessor during the first time cycle.

In one of the Lagrangian rotational simulations, 2 additional time history tracers were used to calculate the positions over time of a pair of adjacent master and slave surface nodes on the slide surface to determine how much slippage of the brain occurs during rotation.

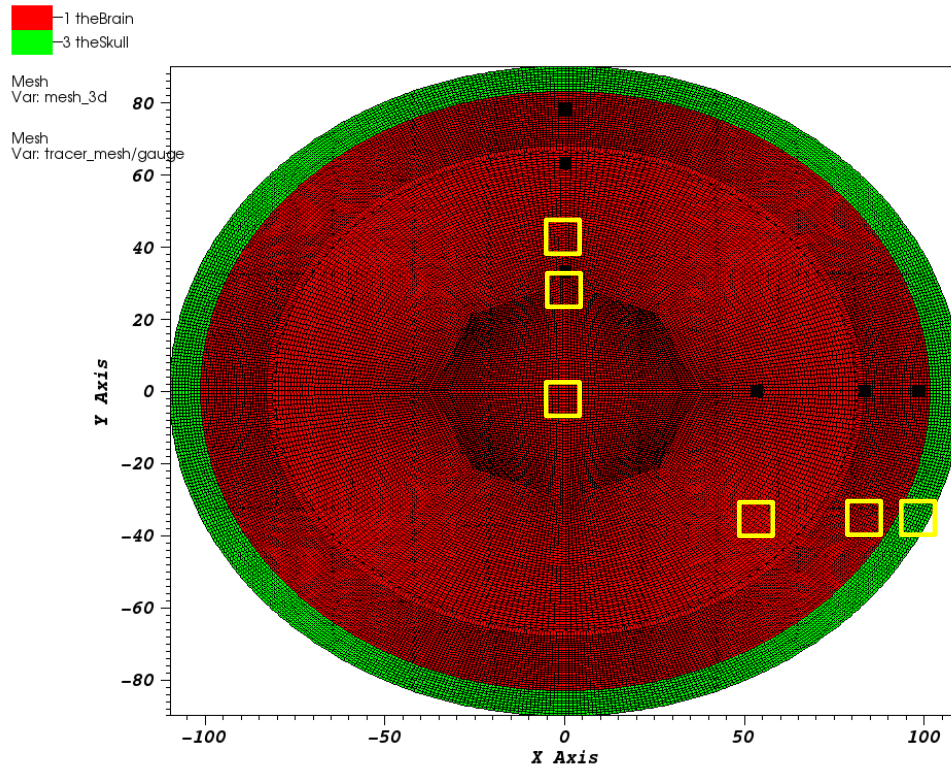


Fig. 6 Locations of tracer particles. The particles are located 5, 20, and 50 mm in from the right and top inner edges of the skull. The example shown is a Lagrangian rotational model. The red and green materials represent the brain and skull, respectively.

Each type of simulation was run at several different mesh resolutions; the average element sizes in the head in each case are given in the following Table. The number of elements given for each simulation is the total number of elements, including background void or air elements, in that simulation. Average element sizes are calculated for the rotation simulations and the Eulerian and embedded blast simulations by finding the percentage area of the head within the mesh and dividing the area of the head by the total number of mesh elements multiplied by this percentage. Average element sizes for the Lagrangian blast simulation were determined by finding the exact number of elements inside the head via temporarily removing the background air and dividing the area occupied by the head by the number of elements; this was done since the mesh resolution of the skull and brain in the Lagrangian blast simulation was much higher than the mesh resolution of the air. Since the embedded simulations and the Lagrangian blast simulation had to be represented in quasi-3-D with a 0.3-mm third-dimensional thickness, the element sizes given are the hypothetical sizes of their 2-D counterparts.

Table. Average element sizes within the head by simulation

Rotation			Blast		
Lagrange	No. of Elements	Avg. Size (mm ²)	Lagrange	No. of Elements	Avg. Size (mm ²)
	44,460	0.700		22,272	1.969
	63,540	0.489		49,230	0.921
	200,928	0.155		94,464	0.420
	393,120	0.079		152,874	0.247
	786,420	0.040		311,994	0.114
Euler	No. of Elements	Avg. Size	Euler	No. of Elements	Avg. Size
	40,000	1.690		101,250	3.997
	90,000	0.751		405,000	0.999
	160,000	0.423		911,250	0.444
	250,000	0.270		1,620,000	0.250
	360,000	0.188		2,531,250	0.160
Embedded	No. of Elements	Avg. Size	Embedded	No. of Elements	Avg. Size
	27,576	2.942		101,538	3.986
	62,190	1.304		405,768	0.444
	111,072	0.730		912,018	0.250
		1,620,768	0.160
		2,532,018	0.999

3. Rotational Model Analysis

3.1 Results across Discretization Methods

The distributions of the pressures, von Mises equivalent stresses, and effective strains in the brain at fixed angles of rotation were drastically different among the discretization schemes, as shown in Figs. 7–9. Again, the embedded simulation was run on a smaller time scale than the Lagrangian and Eulerian models. Also, the embedded model was rotated through atmospheric pressure to satisfy the requirement of the embedded calculations; thus, the range of the pressures and Von Mises equivalent stress for the embedded simulation shown in Figs. 7–9 has been adjusted for an initial internal pressure of 0.101325 MPa. The effective strain rate was given by the following equation:

$$\text{eff. strain} = \sqrt{\frac{2}{3}(\epsilon_{11}^2 + \epsilon_{22}^2 + 2\epsilon_{12}^2)} . \quad (2)$$

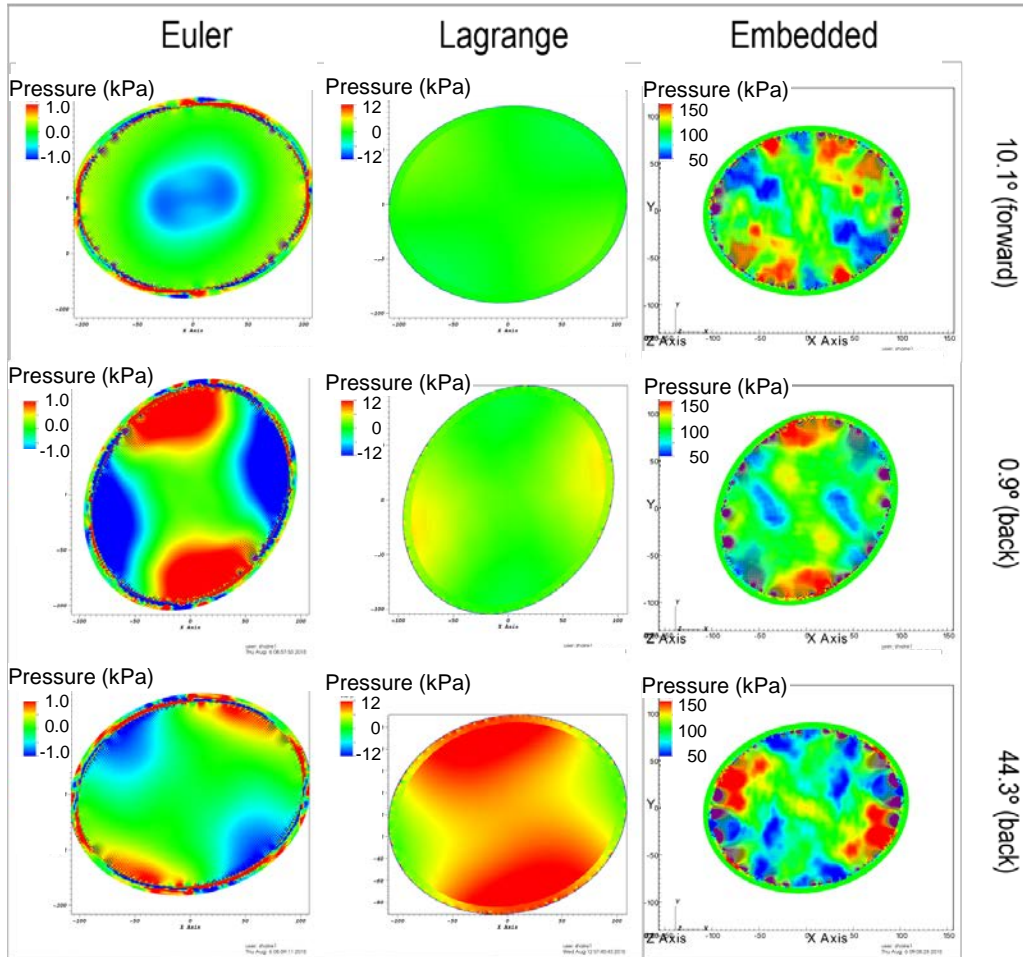


Fig. 7 Effect of discretization method on pressure distribution. The rotation angles shown are 10.1° from equilibrium, 0.9° back toward equilibrium from the inflection point (displaced 59.1° from equilibrium), and 44.3° back toward equilibrium from the inflection point (displaced 15.7° from equilibrium).

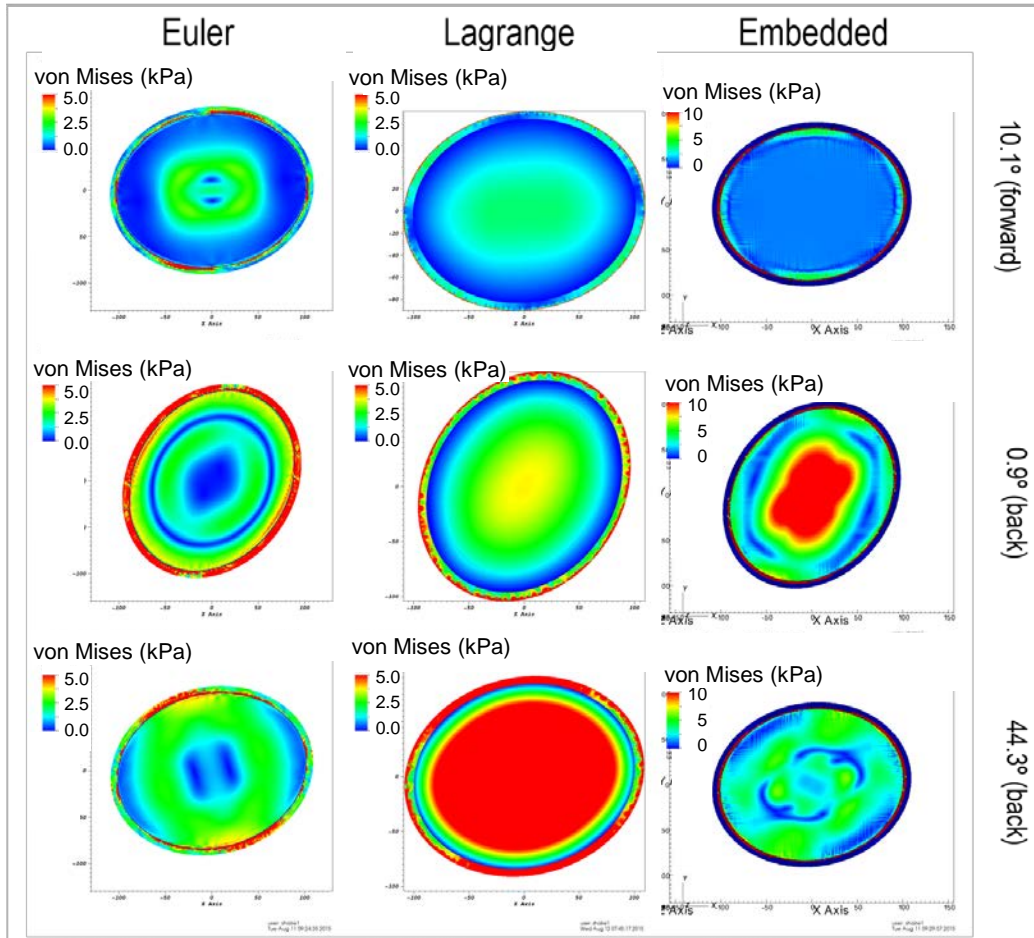


Fig. 8 Effect of discretization method on von Mises equivalent stress distribution. Like in Fig. 7, the rotation angles shown are 10.1° from equilibrium, 0.9° back toward equilibrium from the inflection point (displaced 59.1° from equilibrium), and 44.3° back toward equilibrium from the inflection point (displaced 15.7° from equilibrium).

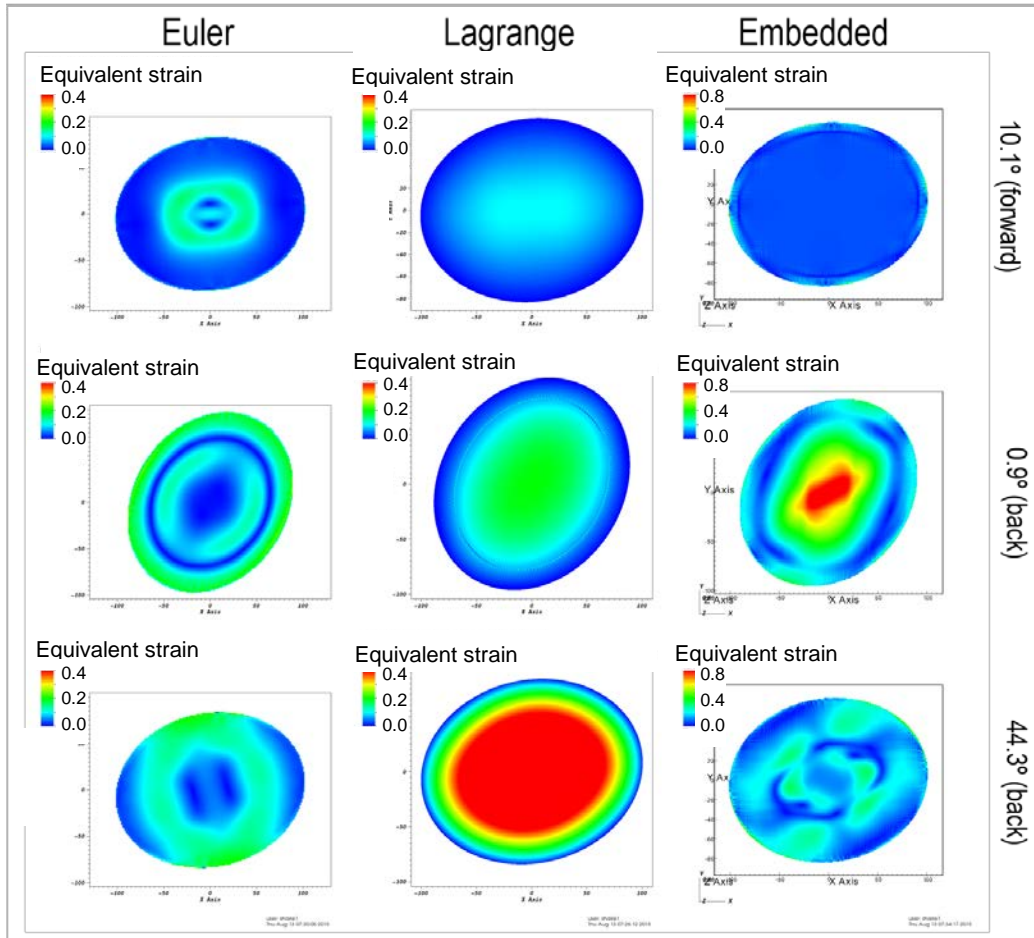


Fig. 9 Effect of discretization method on effective strain distribution. Like in Figs. 7 and 8, the rotation angles shown are 10.1° from equilibrium, 0.9° back toward equilibrium from the inflection point (displaced 59.1° from equilibrium), and 44.3° back toward equilibrium from the inflection point (displaced 15.7° from equilibrium).

One immediately visible result is that the pressure, stress, and strain waves propagating through the brain take on different shapes and frequencies in each case. In the Eulerian and embedded grid models, the pressure waves, Fig. 7, cause peak pressures to arise more interior to the brain than in the Lagrangian case. The embedded grid model, although unfortunately under-resolved because of the time constraints of this study, gives the closest results to the Uintah fixed-grid simulation. The Lagrangian model, oddly, appears not to have a clearly defined pressure wave but has pressures and stresses that gradually build up over time, as would be expected in a problem involving rigid body rotation. Figure 10 plots the distance between nodes in a master/slave node pair over time; the distance is coherent with what would be expected of a fluid rotating within a solid shell.

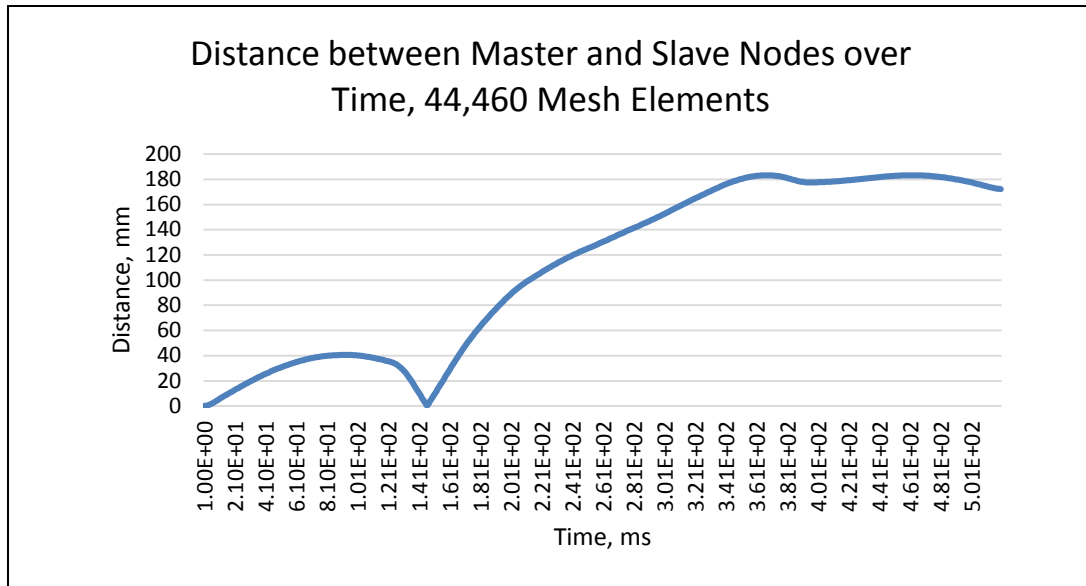


Fig. 10 Distance between master and slave nodes over time

An analysis of what causes pressures to build instead of reflect in the Lagrangian model is ongoing, but the preliminary investigation has shown that the pressure increase can be completely attributed to volume changes in the brain. The change in energy at all time steps in our simulations is zero, so none of the volume changes are due to thermal expansion. It may be the case that the volume changes are due to roundoff error in our boundary conditions that causes the skull to change shape.

Another immediately visible result is that the pressures in the brain in the Lagrangian model are at least an order of magnitude higher than the pressures in the Eulerian model. The magnitudes of pressures observed in the embedded grid model cannot be subject to comparison with the other 2 methodologies because of the shorter timescale over which rotation was applied. The scattered pressures within the skull in the Eulerian model arise from the exterior skull material used to rotate the head.

One notable result is that the highest von Mises stresses and effective strains in all cases occur very near to the center of the brain. This differs from the experimental results and brings up a number of questions as to why this phenomenon arises in our models. The most likely explanation for this is the geometry chosen for our simulations. The simplified, elliptical geometry chosen for our simulations neglects the folds and lobe patterns within a real brain structure. These folds and lobes provide a mechanism similar to hundreds of slide surfaces via which shear stresses arising from the rotation of the brain/skull interface are prevented from propagating far into the center brain. Without those folds and lobes providing a built-in mechanism for slip, the greatest shearing will occur at the center of the brain.

A concerning phenomenon present in the embedded grid model that is not well depicted by Fig. 7 is slight pressure loss and subsequent recovery over the course of the simulation. Visual analysis of results from the simulation show that by the time the brain reaches an inflection point, the average pressure in the brain has dropped by at least 0.02 MPa (the pressure has decreased to at least 80% of initial pressure). All pressure is regained by the end of the simulation; however, the distortion in results that this generated requires an understanding of what in the embedded grid method is causing this pressure flux. One hypothesis is that the reconstruction of the brain/skull boundary in the embedded calculations is subject to roundoff errors when rebuilding element volumes. Small losses in skull volume or stretching of the skull in the radial direction (and thus a miniscule volume increase in the brain) would likely lead to unexpected and unwanted pressure fluctuations. Another hypothesis is that the boundary conditions applied to the skull distort the shape of the skull and cause it to expand slightly; this phenomenon is similar to what we are currently investigating in the Lagrangian simulation, which is subject to comparable loading conditions.

3.2 Effects of Mesh Resolution on Results

Within discretization methods, it was often the case that the resolution of the mesh greatly affected the magnitudes and distributions of the results given by our models. An effect of mesh resolution on the Lagrangian simulations was that the magnitudes of the pressures observed varied significantly with resolution. Peak pressures at some points increased as resolution increased, and others did not. Figure 11 plots the pressures observed at 3 of the tracer locations at 3 different mesh resolutions over time.

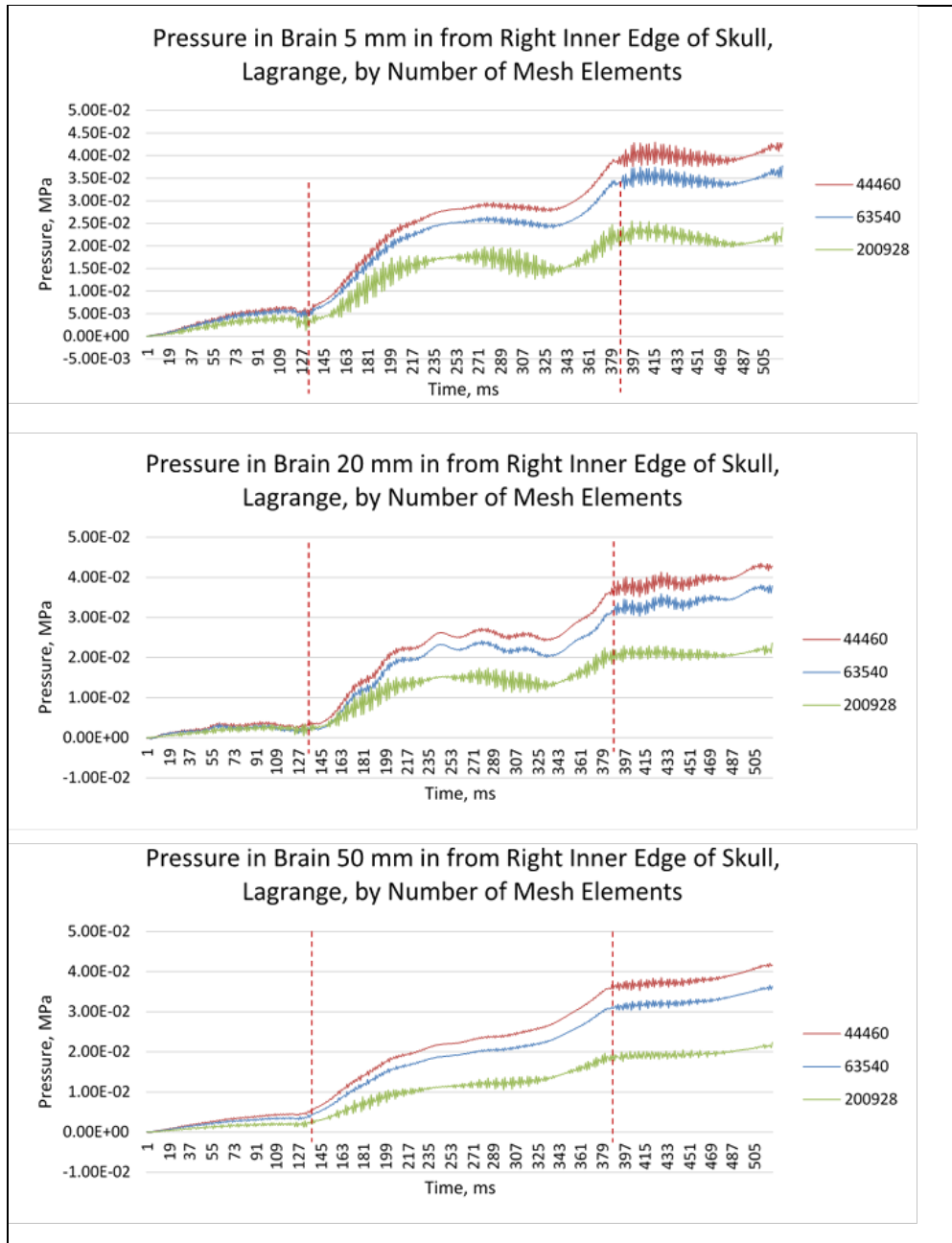


Fig. 11 Pressure over time by mesh resolution at 3 tracer locations, Lagrangian model. The graph legends indicate the number of elements used in each simulation. The red dashed lines display the inflection points in the simulation—that is, the approximate points at which the velocity changed directions. Data points were collected every 1.0 ms.

The peak pressure patterns and magnitudes, although not entirely congruent, are generally consistent across mesh resolutions and show a trend toward a lower-pressure magnitude than is given by our simulations. In all cases, as one nears the center of the brain, the order of magnitude of the pressure values decreases slightly, as would be expected for a rotating body. The remarkable uniformity in shape of the curves shows that not all the pressure effects are mesh related and that our model is capturing the physics of rotation of our head model without much interference. The resultant pressures in the Lagrangian rotational models are all an order of magnitude higher than the corresponding pressures in their Eulerian and embedded counterparts. As mentioned previously, the steady increase in pressures is completely dependent on changes in the volume of the brain that may in turn result from errors in our rotational boundary conditions; investigation into the cause of the volume change is ongoing.

In the Eulerian simulations, the peak pressure values were similar to each other, but the times at which peak values were reached differed. Also, at locations closer to the skull, the pressure patterns observed were inconsistent across resolutions. However, like the Lagrangian simulations, the pressure curves appear to be converging to a single result as mesh resolution increases. Figure 12 displays this phenomenon.

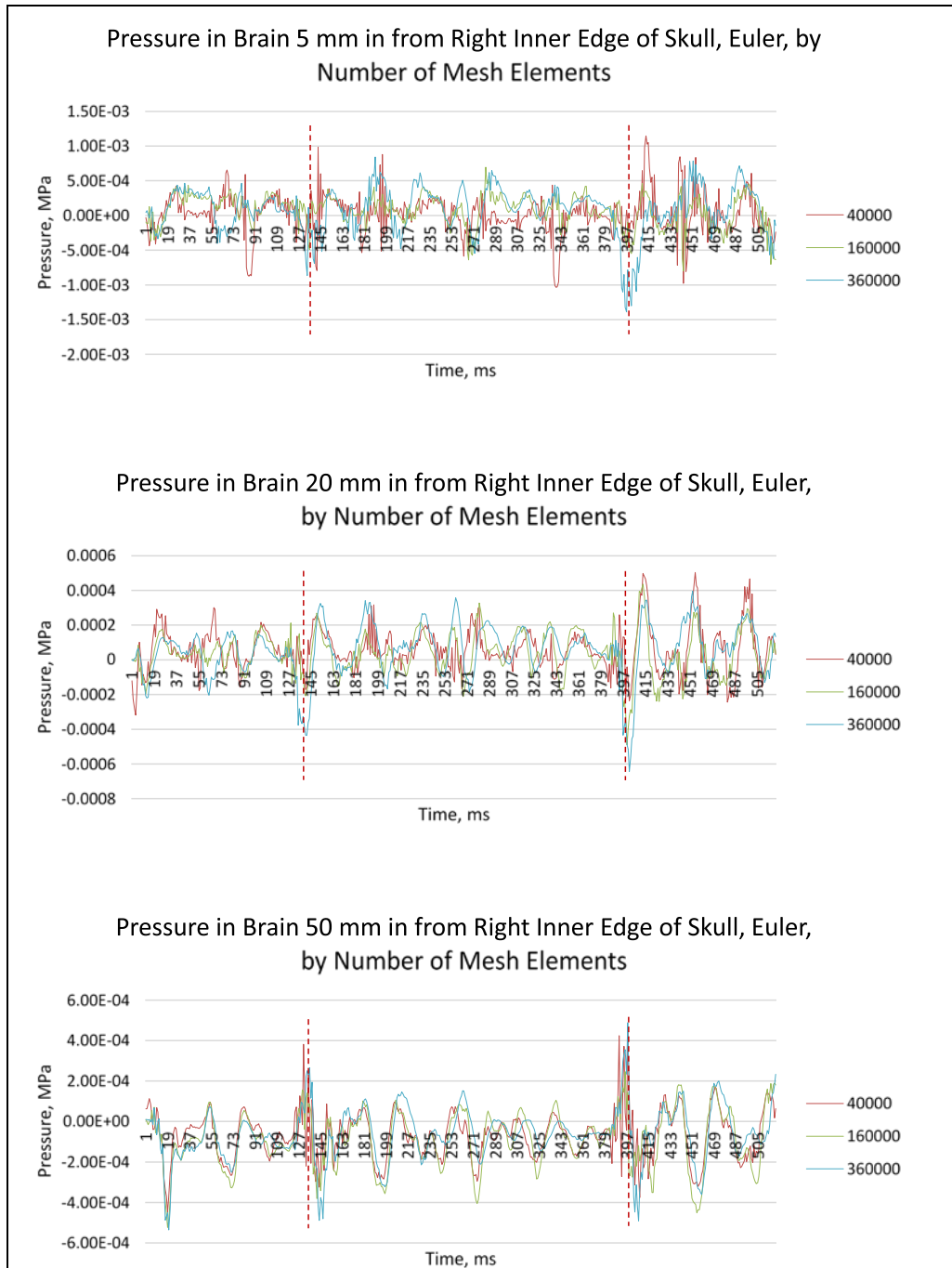


Fig. 12 Pressure over time by mesh resolution at 3 tracer locations, Eulerian model. As in Fig. 11, the graph legends indicate the number of elements used in each simulation, and the red dashed lines display the inflection points in the simulation—that is, the approximate points at which the velocity changed directions. Data points were collected every 1.0 ms.

For the Eulerian simulations, the primary effect of mesh resolution appears to be the phase of the pressure curve as opposed to pressure magnitudes, and the phases become more in agreement among the models as one nears the center of the brain. Since the Eulerian method averages material properties over mixed-material elements (in our model, along the skull/CSF/brain boundary, which the 5-mm tracer was very close to), mesh resolution would be expected to be a large factor in the results along boundaries between materials and virtually a nonfactor far from mixed-material elements. As mesh resolution increases, the area over which averaging occurs decreases, potentially improving the accuracy of the Eulerian model. One of the most important pieces of Fig. 12 is that the boundary effects propagate toward the center of the brain; across resolutions, the highest pressures were located 20 mm from the skull as opposed to the normally expected 5 mm from the edge of the skull.

In creating Figs. 11 and 12, sets of results for 5 different mesh resolutions were initially plotted, but this number was reduced to 3 to allow for better visualization of results. The high, low, and middle resolutions were kept in the graphs.

The unfortunate effects of under-resolution are manifested in the comparison of embedded grid results across mesh resolutions as shown in Fig. 13. Note that the zero pressure for these simulations is atmospheric pressure instead of 0.0 MPa.

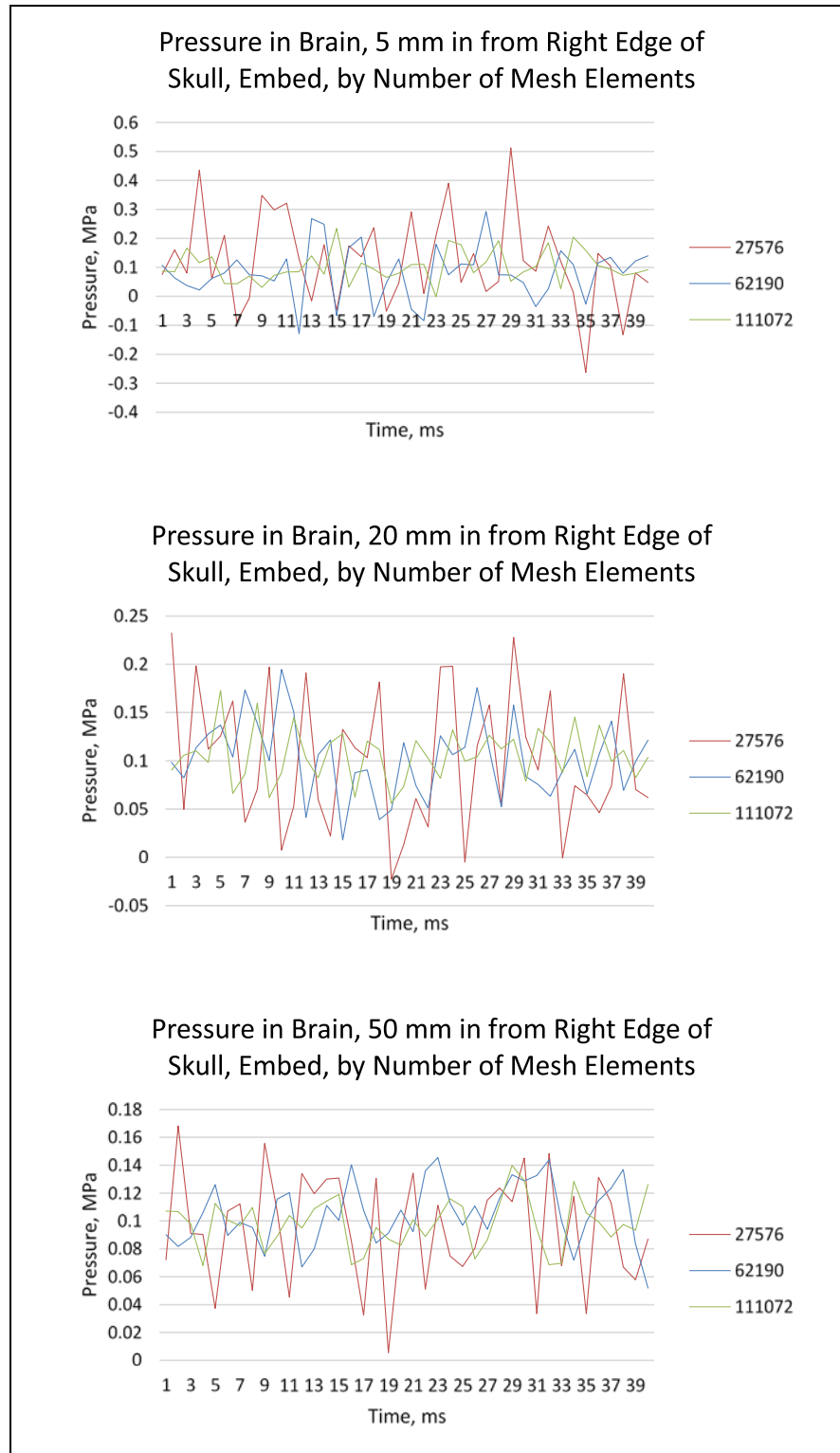


Fig. 13 Pressure over time by mesh resolution at 3 tracer locations, embedded model. As in Figs. 11 and 12, the graph legends indicate the number of elements used in each simulation. Data points were collected every 1.0 ms.

The steepness of the spikes and drops in this figure seen in the meshes with lower resolutions can be attributed mainly to the checkerboarding in the simulation that resulted from the low mesh resolution. The amplitudes of the peaks decrease with increasing mesh resolution, implying that the simulations are converging to a gentler pressure curve that hovers very near atmospheric pressure. Like the Lagrangian simulations, the highest pressures seen in the embedded grid simulations are at the very outside of the brain.

3.3 Efficiency Analysis

The efficiencies of each discretization type with respect to simulation size are difficult to compare across all 3 methods; however, some analysis can be performed. Figure 14 displays the wall times of the Lagrangian and Eulerian simulations with respect to mesh resolution. All simulations were run on Excalibur on 64 processors.

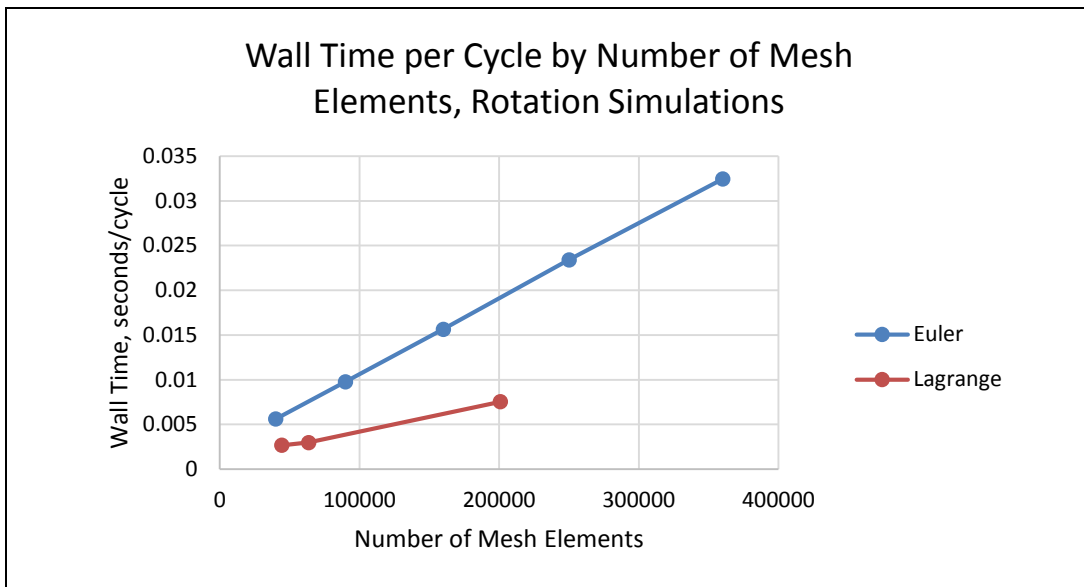


Fig. 14 Wall time by mesh resolution of Lagrangian and Eulerian methods, rotational models

In finite element analysis, it is usually expected that Lagrangian simulations run faster than Eulerian simulations because Lagrangian models do not have to account for advection across element boundaries. This is definitely the case for our models, and it appears that both methods provide a nearly linear run time with respect to input (mesh) size. Because of the time constraints of our project, we were only able to obtain results at 3 different mesh resolutions in the Lagrangian case.

Unfortunately, because of the constraints of our simulations and the necessary restarts that had to be performed, the exact recorded wall times of the embedded simulations were lost. However, we can approximate that the embedded simulation with 111,072 elements ran for about 46 h to reach 40.0 ms; the Lagrangian simulation with approximately twice that many elements ran for around 14 h to reach 520.0 ms. The inefficiency posed by the embedded model was a major limiting factor on the quality of results available for this study.

4. Blast Loading Model Analysis

4.1 Results across Discretization Methods

Figure 15 depicts the results of the blast loading simulations using each discretization method at the highest resolution we were able to run.

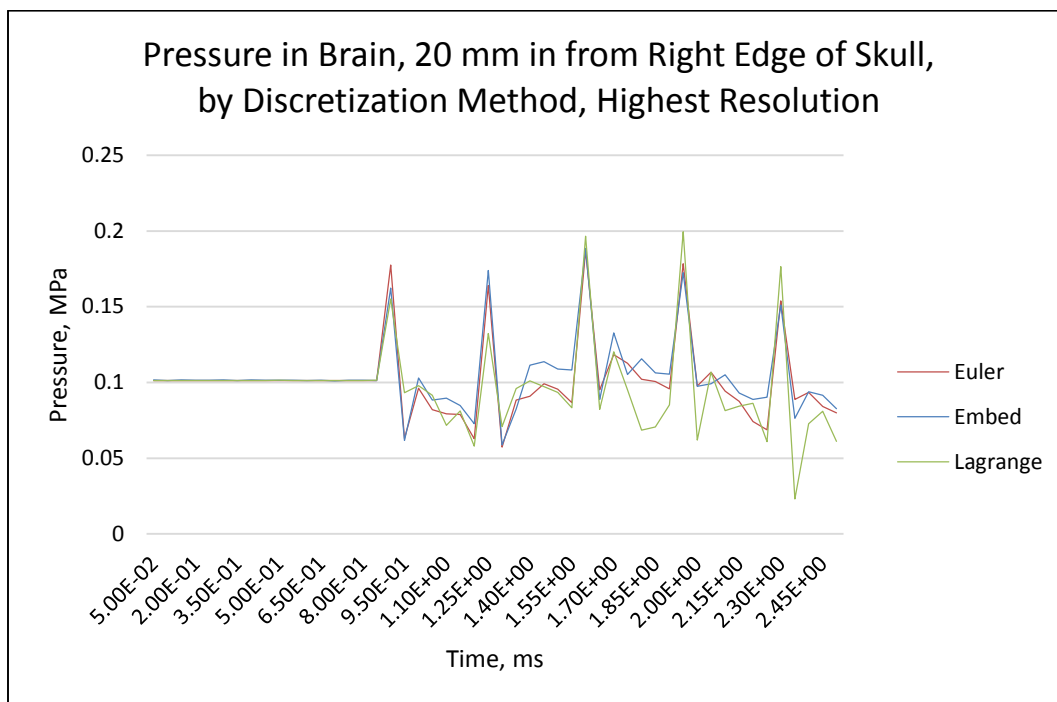
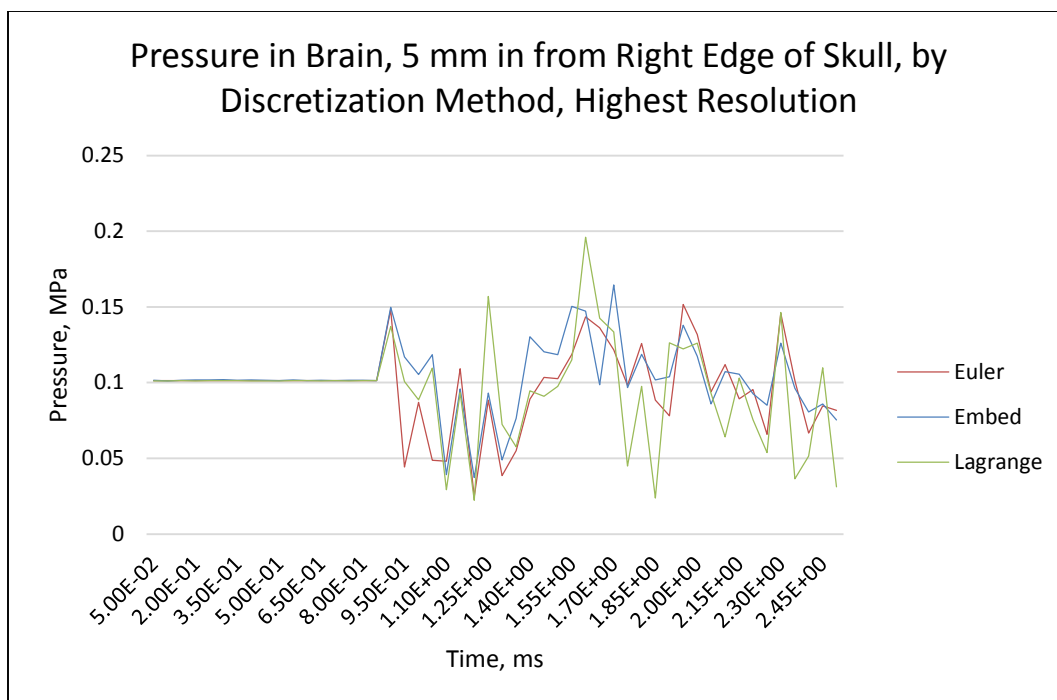


Fig. 15 Pressure over time by discretization method at 6 tracer locations, highest resolution. The number of elements in the Eulerian, embedded, and Lagrangian simulations are 2,531,250; 2,532,018; and 311,994; respectively. Data points were collected every 1.0 ms.

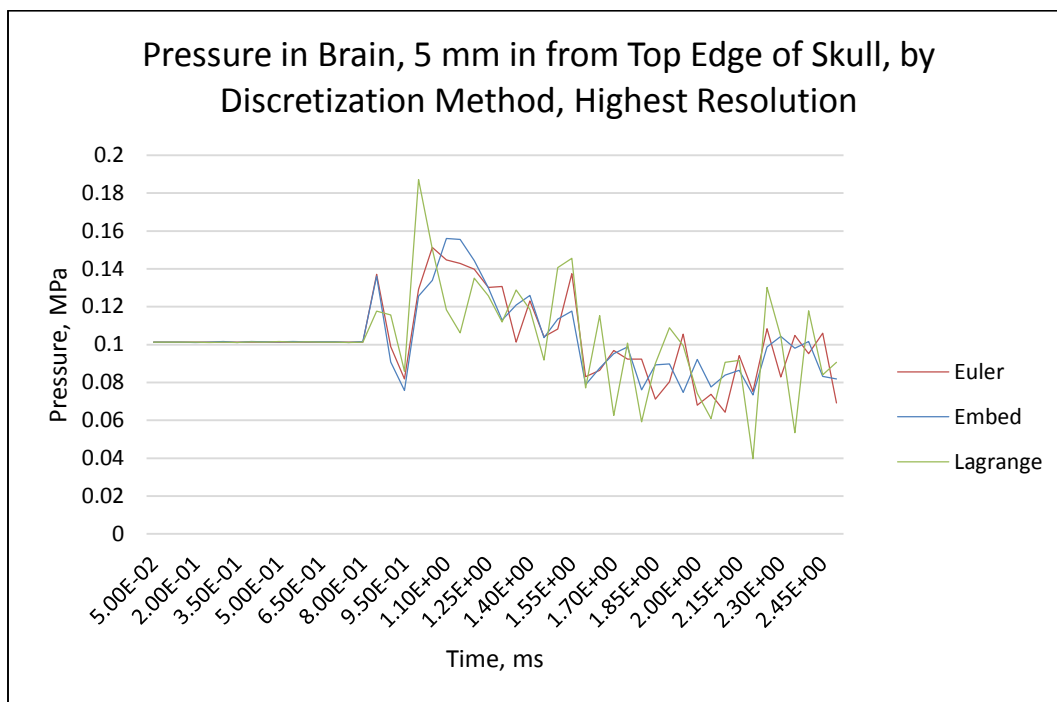
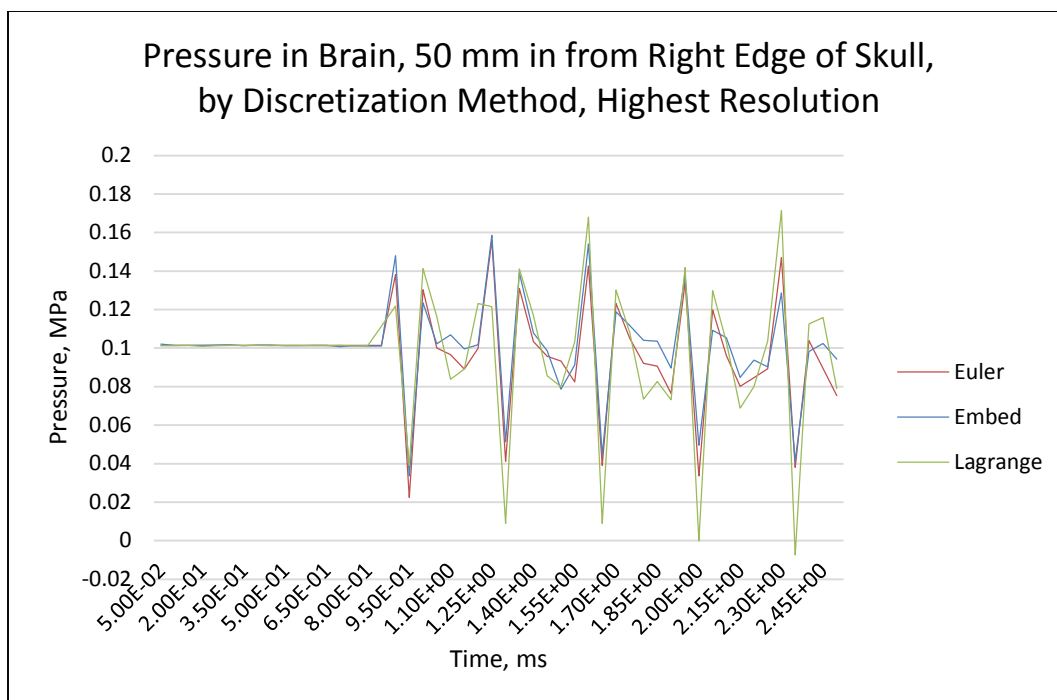


Fig. 15 Pressure over time by discretization method at 6 tracer locations, highest resolution. The number of elements in the Eulerian, embedded, and Lagrangian simulations are 2,531,250, 2,532,018, and 311,994, respectively. Data points were collected every 1.0 ms (continued).

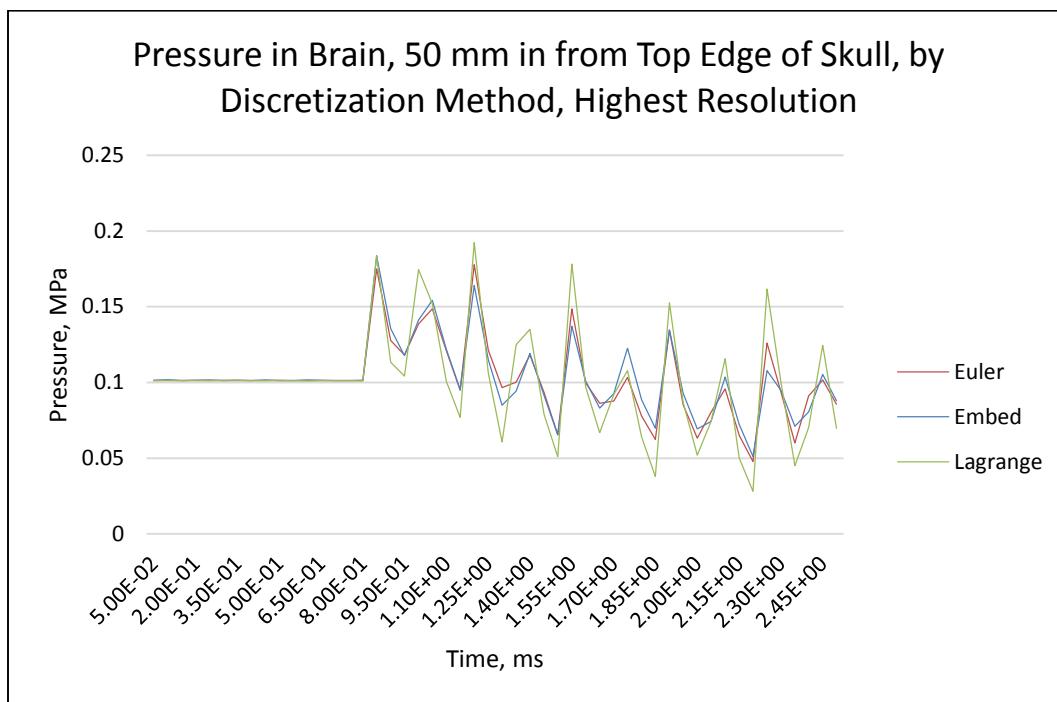
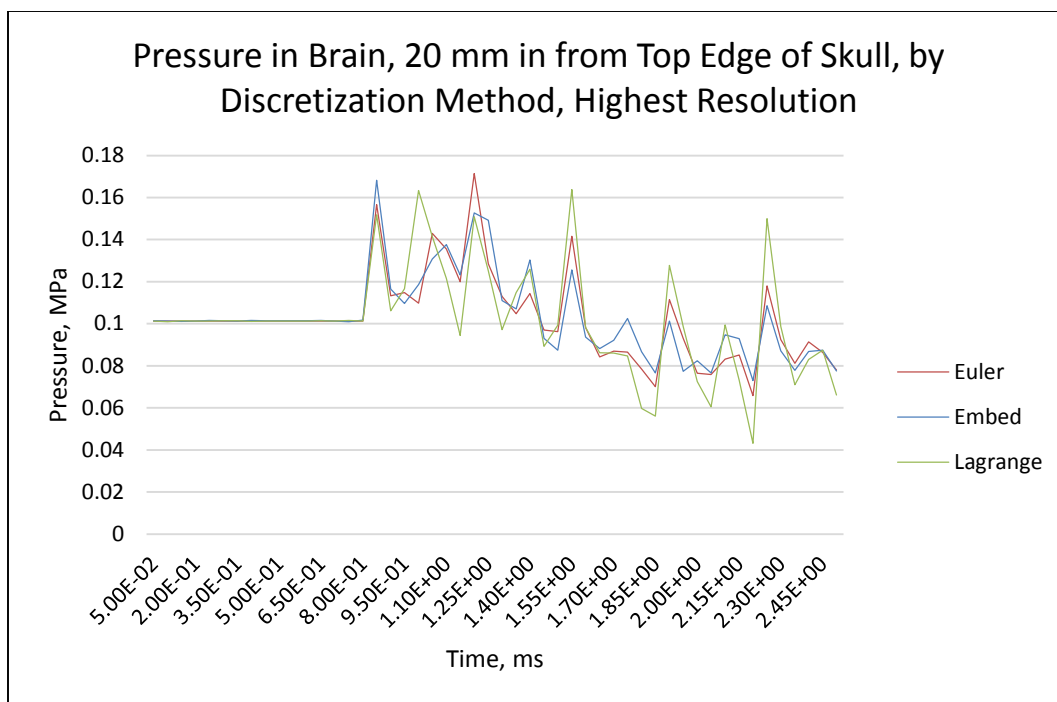


Fig. 15 Pressure over time by discretization method at 6 tracer locations, highest resolution. The number of elements in the Eulerian, embedded, and Lagrangian simulations are 2,531,250, 2,532,018, and 311,994, respectively. Data points were collected every 1.0 ms (continued).

Unlike in the rotation problem, the magnitudes and distributions of pressures in the blast loading simulations across discretization schemes were remarkably similar. Each simulation clearly showed 5 distinct pressure wave reflections within the skull over the course of the simulation; these reflections were observed at almost identically the same times and in the same places in each case. The magnitudes of pressures never deviated from atmospheric pressure by more than 0.1 MPa in any of the cases. The primary differences among the sets of results lie at the points closest to the brain/skull interface, as expected. The embedded grid methodology displays the shallowest wave peaks along the edge of the brain; the air required behind the skull for the embedded model may have had the effect of dampening the pressure wave. The sharpest and tallest wave peaks, as well as clearest pressure modes, are seen in the Lagrangian simulations; since Lagrangian meshing does not have mixed material zones, the averaging of properties seen in the other 2 methodologies may be dampening results by providing a gradient of densities over which the pressure wave has to pass before reflecting.

4.2 Effects of Mesh Resolution on Results

Mesh resolution of the blast loading meshes was not as large a factor in the pressure values recorded over time as it was for the rotational simulations. Figure 16 plots the results for the Eulerian blast loading model.

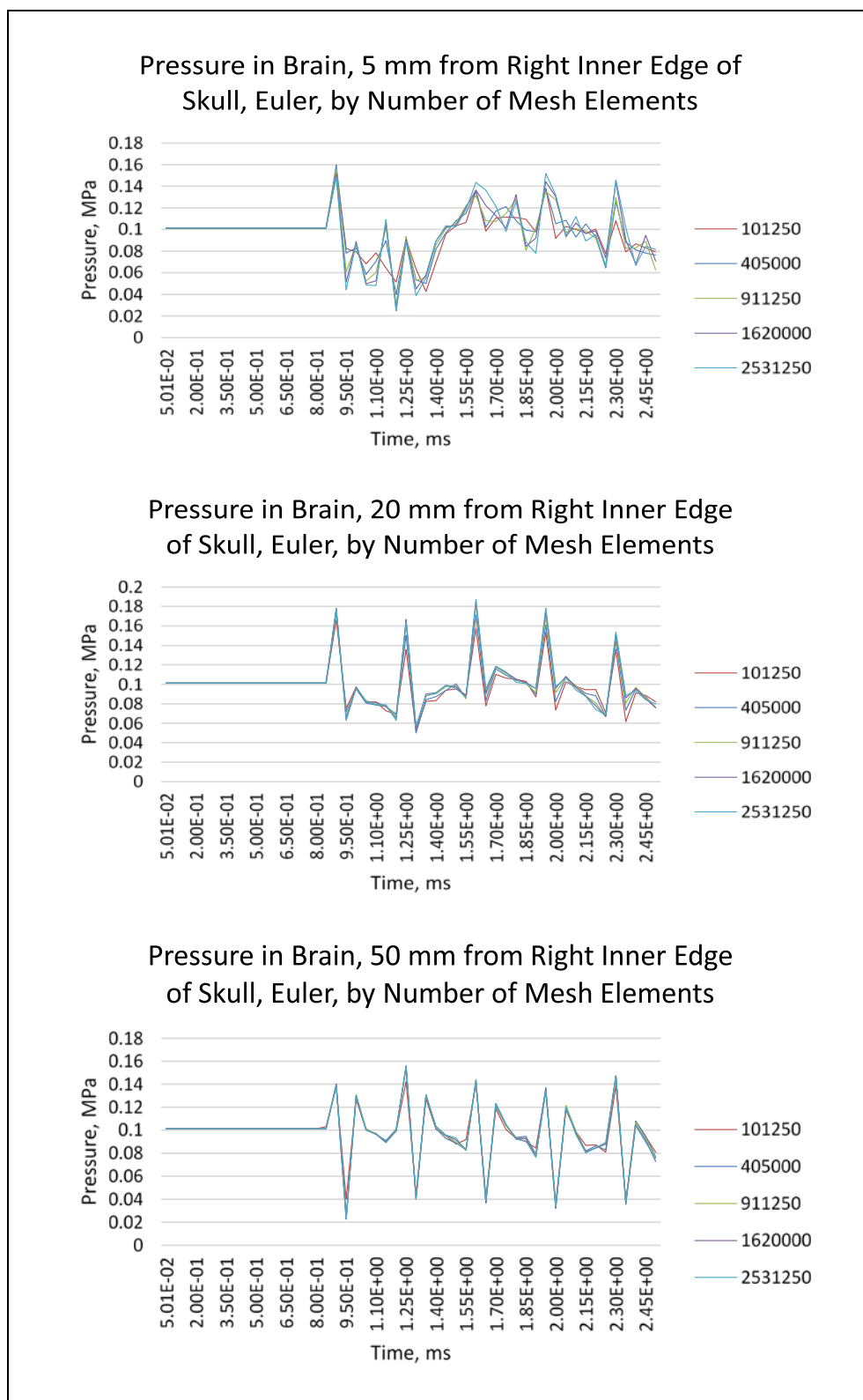


Fig. 16 Pressure over time by mesh resolution at 3 tracer locations, Eulerian blast model. The graph legends indicate the number of elements used in each simulation. Data points were collected every 1.0 ms.

Pressure magnitude and wave reflection timing are extremely consistent across mesh resolutions for the Eulerian simulations. The “shakiness” observed in the values across resolutions at the 5-mm tracer particle is likely due to the mixed-material elements at the brain/CSF/skull interface; finer resolution of the CSF results in mixed elements comprising a smaller portion of the mesh, which should improve the accuracy of the simulation.

Mesh resolution appears to be slightly more of a factor in the embedded simulations’ results, as shown in Fig. 17.

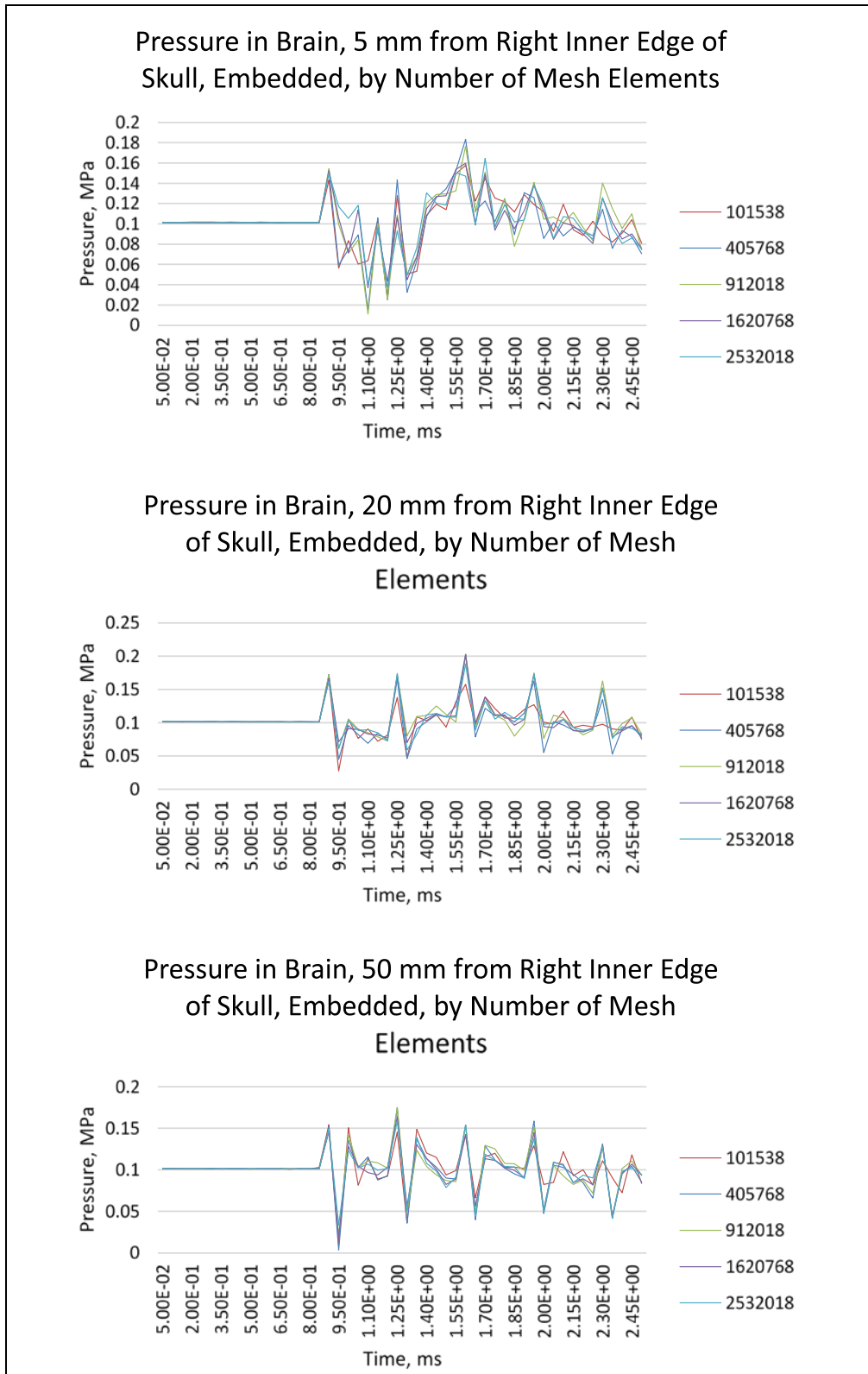


Fig. 17 Pressure over time by mesh resolution at 3 tracer locations, embedded blast model. The graph legends indicate the number of elements used in each simulation. Data points were collected every 1.0 ms.

However, the convergence among the models is still very tight. Like the Eulerian blast simulation, the greatest divergence in pressure values is seen closest to the skull. In the case of the embedded simulation, this may be due to accumulated error in the FEusion calculation that is performed at the brain/skull boundary.

The Lagrangian blast loading models have the greatest results discrepancies with differing mesh resolution (Fig. 18); part of this may be due to the smaller numbers of overall elements than their Eulerian and embedded grid counterparts. The results appear to converge over time toward a clearly defined pattern of 5 wave reflections in the head over the course of the run. Once again, the highest discrepancies are closest to the skull. There are no mixed-material zones in the Lagrangian models; however, embedded grid methods were used to implement the background air, some of which lies behind the skull. It may be that the discretization of this calculation is a large factor in results. Another possible method of implementing the background air is to use a conformal mesh surrounding the head with a slide surface between the air and the skull. Unfortunately, there was not enough time available to create a conformal mesh during this study. Further investigation into different methods of implementing the background air would be required to understand this phenomenon more fully.

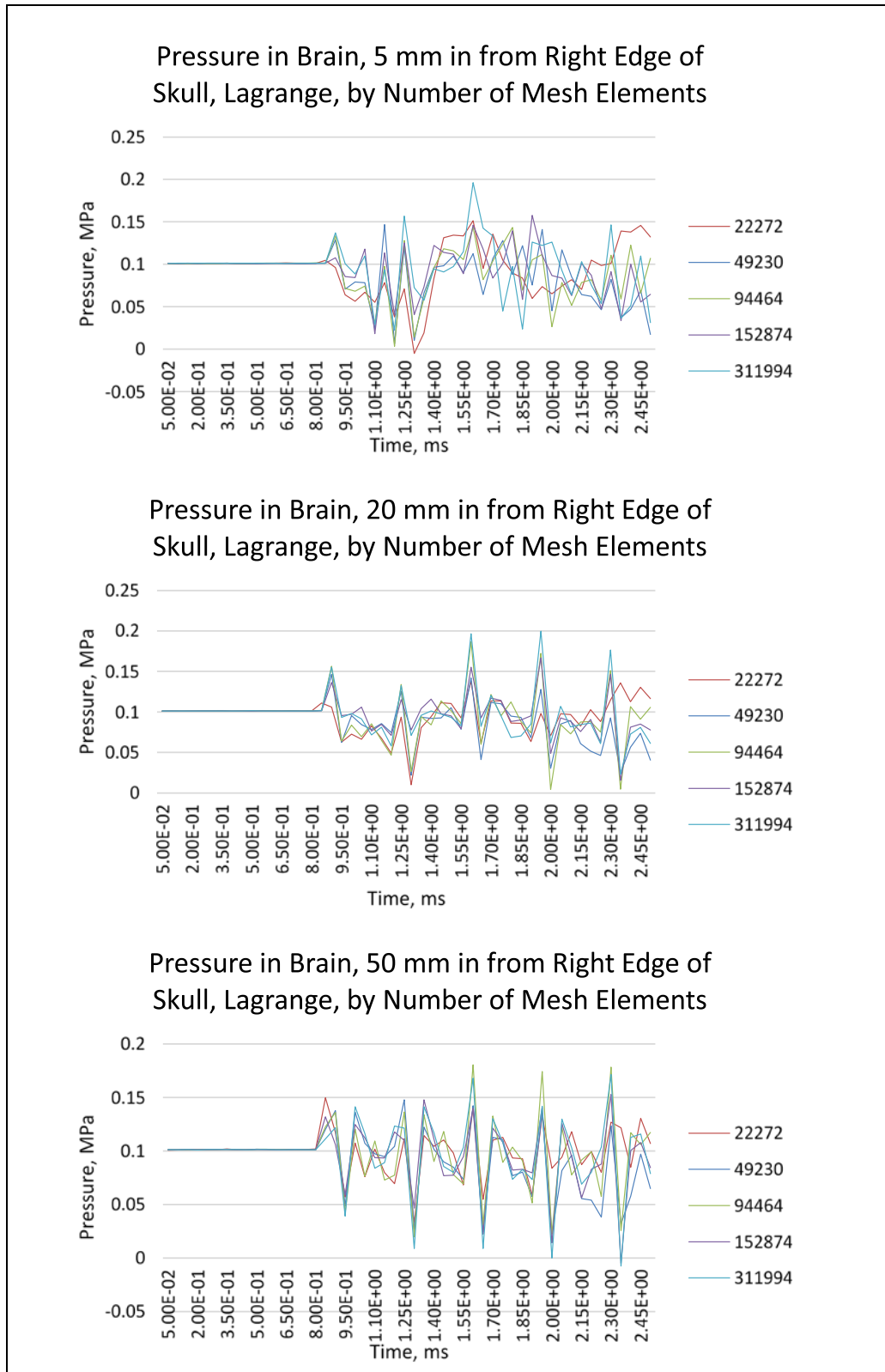


Fig. 18 Pressure over time by mesh resolution at 3 tracer locations, Lagrangian blast model. The graph legends indicate the number of elements used in each simulation. Data points were collected every 1.0 ms.

4.3 Efficiency Analysis

An interesting piece of the blast loading simulations is that contrary to what is normally expected in modeling, the Lagrangian simulation appears to be the least efficient for the number of mesh elements used (Fig. 19). This is probably due to the use of embedded grid methods to provide the background air for the run; it is recommended that a methodology that does not use an embedded methodology be implemented for the Lagrangian run. However, the Lagrangian simulations only required one embedded interface (between the skull and air), while the embedded simulations required 2 embedded interfaces (between the skull and air and between the brain and skull). In this planar situation, the Eulerian model is by far the quickest run.

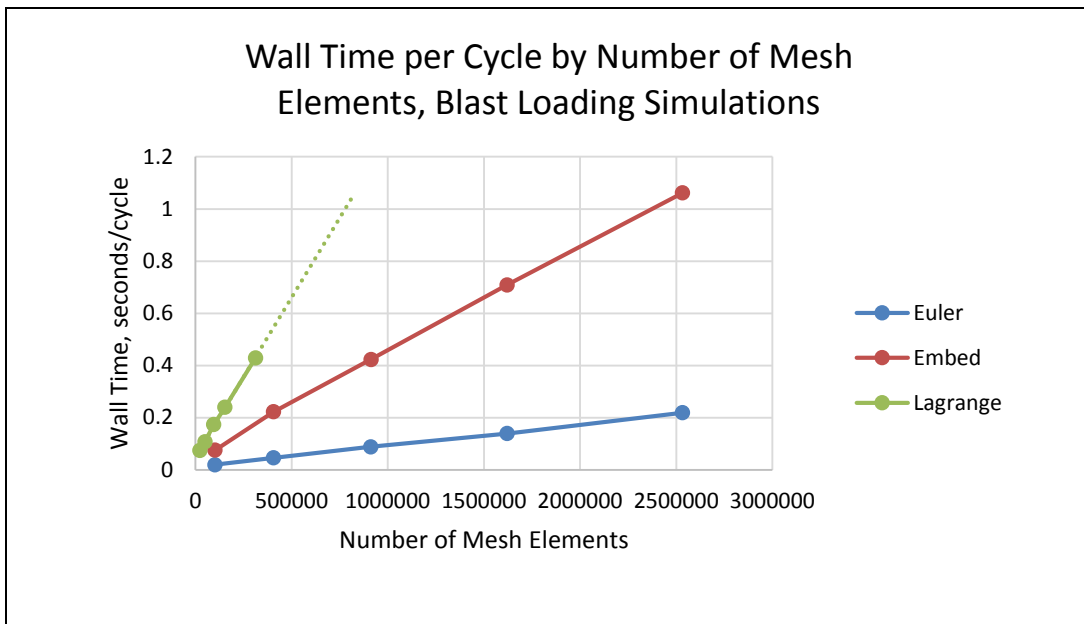


Fig. 19 Wall time by mesh resolution of each discretization method, blast models. For clarity, a projected linear trend curve is included for the Lagrangian model.

5. Conclusions and Recommendations

We have seen that in under both rotational and blast loadings, brain trauma simulation results are significantly affected by the discretization method used in creating the mesh. In the rotational problem, results using the same boundary conditions were disparate; there were little similarities among the pressure wave patterns observed in each case. The embedded grid model appears to have the most spatially similar pressure patterns to the data from human trials.¹ However, although the preliminary results of the method look promising, the pressure loss during the simulation and the extremely long run times of the model make it less

than desirable for the application we have presented. Investigation into the cause of the pressure loss and into techniques that improve the efficiency of the simulation are of paramount importance for future use of the embedded method in cases when the foreground and background meshes slide against each other. Also, the embedded model's usefulness was limited by the low mesh resolutions required to complete the simulations on time; for further investigation, it is essential that a finer embedded mesh be used. The Lagrangian rotational simulation requires further study as well to determine the cause of the volume change that results in a pressure buildup that deviates from expected results. Our hypothesis is that the volume change results from error in the boundary conditions, but this hypothesis requires verification.

The most pressing topic for further investigation across all methods is the effect of brain structure on the propagations of pressures, stresses, and strains. It is expected that a geometry which accurately represents the folds and lobes of the brain will have enough internal sliding mechanisms that the shear stresses will remain highest on the outside of the brain, which is very different from our results. For the blast loading problem, all 3 methods perform similarly and efficiently in areas far from the skull. An appropriate next step would be to conduct a study that provides a clearer physical explanation for the discrepancies in results near the brain/skull interface. Also, methods to implement the Lagrangian model that do not use embedded techniques to implement the air are of interest in future work both to isolate the Lagrangian method within the simulation and to improve the model's run time. Unlike the rotational problem, it is not anticipated that incorporating an accurate brain geometry will affect results since no shear forces are involved in the simulation.

6. References

1. Daphalapurkar N, Ganpule S. Presentation: Dynamic shearing deformations in living human brain: modeling and validation. Baltimore (MD): The Johns Hopkins University. Presented to the Soldier Protection Sciences Branch, US Army Research Laboratory, Aberdeen Proving Ground, MD; 2015 Feb.
2. Nichols AL, editor. ALE3D users' manual, arbitrary Lagrangian-Eulerian 3D and 2D multi-physics code. Livermore (CA): Lawrence Livermore National Laboratory; 2015 Sep. Report No.: LLNL-SM-662355.
3. Huang Y. Simulation of blast on a porcine head. Aberdeen Proving Ground (MD): Army Research Laboratory (US); 2015 July. Report No.: ARL-TR-7340.
4. Fitzpatrick R. Designing and constructing an animatronic head capable of human motion programmed using face-tracking software [master's thesis]. [Worcester (MA)]: Worcester Polytechnic Institute; 2010 May 1.
5. Stewart J. US Army Research Laboratory, Aberdeen Proving Ground, MD. Personal communication, July 2015.

INTENTIONALLY LEFT BLANK.

Appendix. Material Parameters

This appendix appears in its original form, without editorial change.

Approved for public release; distribution is unlimited.

Void

```
voidinput ss0 1000
```

Air

```
matinput
  czero 2.0 qfb 0.0 crq 0.1 pmin -1.0e-01
  eosvmin 1.0e-03 eosvmax 1.0e+03 vhlmit 1.0e+05
  rho 1.18e-6      cvav {(720.)*(1.18e-6)} p0eosvmax 1
evfrom tp
  p0 1.01325e-1
  t0 298.
  e0 2.533125e-01
  v0 1.0
koinput
  isol 0 iform 5
  coef 0.4
```

Brain

```
matinput
  rho 1.04e-3  e0 0.0  v0 1.0
  pmin -2.0e2      epsfail 25
  czero 2.0  crq .1  qfb 0.15      linq 1
  cvav 2.926  eosvmin 0.3  eosvmax 2.0
  t0 300.0

msinput
ysmodel 146
  shr_mod 13.e-3  w0 0.3      order 2  adv_log 1
elamodel 99
hardmodel 299
eosmodel 304
  rhoc2 2200  s1 2.56  s2 -1.986  s3 .2268  g0 0.5 a 0.
  eosvmin 0.3  eosvmax 2.0
  ec0 -877.8
  em0 800.
failmodel 499
```

Cerebrospinal Fluid

```
# y0 from Bloomfield et. al., 1998 -> assumed viscosity and
density of water
```

```
matinput
  rho 1.04e-3  e0 0.0  v0 1.0
  pmin -2.0e2      epsfail 25
  czero 2.0  crq .1  qfb 0.15      linq 1
  cvav 2.926  eosvmin 0.3  eosvmax 2.0
  t0 300.0
```

```

msinput
ysmodel 100
elasmodel 0
shr_mod 2660
hardmodel 201
    y0 8.9e-7 ybet 0 n 0.1 ymax 5 rate_a 0 rate_b 1
    rate_exp 1
eosmodel 304
    rhoc2 2200 s1 2.56 s2 -1.986 s3 .2268 g0 0.5 a 0.
    eosvmin 0.3 eosvmax 2.0
    ec0 -877.8
    em0 800.
failmodel 499

```

Skull

```

matinput
    rho 1.412e-3 e0 0.0 v0 1.0
    cvav 3.772

msinput
ysmodel 100
elasmodel 0
    shr_mod 2660
hardmodel 201
    y0 4 ybet 0 n 0.1 ymax 5
eosmodel 304
    rhoc2 3891 s1 0.94 s2 0 s3 0 g0 1.0 a 0.
    ec0 -1131.6
    em0 800.
failmodel 499

```

1 DEFENSE TECHNICAL
(PDF) INFORMATION CTR
DTIC OCA

2 DIRECTOR
(PDF) US ARMY RESEARCH LAB
RDRL CIO LL
IMAL HRA MAIL & RECORDS
MGMT

1 GOVT PRINTG OFC
(PDF) A MALHOTRA

1 UMBC
(PDF) S HAIRE

10 DIR USARL
(PDF) RDRL WMP A
S R BILYK
RDRL WMP B
C HOPPEL
Y HUANG
S SATAPATHY
S WOZINAK
A SOKOLOW
RDRL WMP C
R BECKER
T BJERKE
RDRL WMP G
S KUKUCK
R EHLERS